Scripta Materialia 219 (2022) 114888

Contents lists available at ScienceDirect

Scripta Materialia

journal homepage: www.journals.elsevier.com/scripta-materialia

Structure and substructure characterization of solution-treated $Ni_{50.3}Ti_{29.7}Hf_{20}$ high-temperature shape memory alloy

Jiaqi Dong *, Tejas Umale, Benjamin Young, Ibrahim Karaman, Kelvin Y. Xie *

Department of Materials Science and Engineering, Texas A&M University, College Station, TX 77843, USA

ARTICLE INFO

Keywords:
Shape memory alloys
Martensite
Twinning
Scanning/transmission electron microscopy

ABSTRACT

We investigate the structure and substructure of the solution-treated martensitic $Ni_{50.3}Ti_{29.7}Hf_{20}$ high-temperature shape memory alloy (SMA) by transmission electron microscopy and precession electron diffraction (PED). Most martensite plates contain high-density internal (0 0 1) compound twins. Four martensite variants (i.e., *A, B, C*, and *D*) were observed using PED. The orientation relationships were determined to be (1 1 0.64) Type II twins between *A* and *B*, and (1 1 1) Type I twins between *C* and *D*. *B* and *C* are divided by junction planes, in which (1 1 1) in *C* is parallel to (1 1 0.64) in *B*. These orientation relationships are rarely observed in other NiTi or NiTiHf SMAs, which offers new insight to understand the phase transformation behavior in $Ni_{50.3}Ti_{29.7}Hf_{20}$ SMAs. Several low-angle grain boundaries were observed near the variant interfaces, which may explain the difficulty of martensite reorientation and detwinning in NiTiHf SMAs.

Shape memory alloys (SMA) are important class of engineering materials due to their ability to exhibit large reversible shape changes as a result of the thermoelastic martensitic transformation. Thus, SMAs are notably used in the automotive, aerospace, and medical industries. NiTi alloys are the most popular SMAs due to their superior shape memory properties, large superelastic strain, and corrosion resistance [1]. However, the operating temperatures of binary NiTi SMAs are below 100 °C, limiting its wider application at high temperatures. Alloying with a ternary element is often used to increase the transformation temperatures (TTs) of NiTi and improve the dimensional stability under actuation loading [2–4]. Compared with other ternary elements leading to higher TTs (e.g., Pd, Pt, Au), the NiTiHf SMAs has a lower cost and higher work output at high temperatures [5]. In NiTiHf SMAs, the TTs increase almost linearly with the Hf content when it ranges from 10 at.% to 30 at.% [6–8]. In addition, TTs are very sensitive to the Ni content beyond 50 at.%, which drop rapidly when the Ni content increases [6,9].

Martensite variant reorientation and detwinning are critical mechanisms that dictate the nature and extent of martensitic transformation and play a significant role in the reversibility of the shape recovery in SMAs. Therefore, it is imperative to understand the characteristics of twinning and inter-twin interfaces in the martensite phase in SMAs. For example, Madangopal et al. and Nishida et al. found these following twin modes in $Ni_{50}Ti_{50}$: <0 1 1> Type II twins, [10] Type I twins, (1 0 0) and (0 0 1) compound twins, and {0 1 1} Type I twins, in which the <0 1 1> Type II twin was predominant [11–13]. For $Ni_{48.5}Ti_{36.5}Hf_{15}$ (a Ni-lean SMA), Han et al. observed (0 0 1) compound twins in martensite variants, which is attributed to the lattice invariant shear transformation [14]. In addition, the two "junction planes" between B19' martensite variants were determined as (0 1 1) and (1 -1 0.64) [14]. For $Ni_{49}Ti_{36}Hf_{15}$ (also a Ni-lean SMA), Zheng et al. observed (0 1 1) Type I, <0 1 1> Type II, and (1 -1 1) Type I twinning [15]. The differences in the twin modes reported by Han et al. and Zheng et al. may be attributed to the slight compositional differences and the processing methods [14,15]. We realized that most martensite characterization of NiTiHf ternary systems has largely focused on the solution-treated Ni-lean samples [15–17] and precipitate bearing Ni-rich samples [10,18-20]. There is a lack of detailed investigations of the martensite characterization of Ni-rich NiTiHf SMAs, especially in the solution-treated condition. Moreover, experimental evidence revealed that NiTiHf SMAs generally exhibit lower transformation strain than NiTi [20–28], in contrast to the theoretical prediction [29]. Hence, it is important to study the martensite structure and substructure to identify which characteristic differences can explain the lower transformation strain in NiTiHf.

In this work, the martensite structure and substructure of the solution-treated $Ni_{50.3}Ti_{29.7}Hf_{20}$ were investigated. $Ni_{50.3}Ti_{29.7}Hf_{20}$ (a Ni-rich ternary SMA) has the ability to form nano-precipitates which help manipulate the TTs, strengthen the material, and enhance the reversibility of phase transformation and dimensional stability upon

* Corresponding authors.
E-mail addresses: djq0420@tamu.edu (J. Dong), kelvin.xie@tamu.edu (K.Y. Xie).

https://doi.org/10.1016/j.scriptamat.2022.114888
Received 11 April 2022; Received in revised form 20 June 2022; Accepted 20 June 2022

cyclic actuation [26,30-33]. Our microstructure characterization on the solution-treated samples serves as a baseline for future studies on the precipitate-bearing $Ni_{50.3}Ti_{29.7}Hf_{20}$ SMAs and for a better comparison with NiTi SMAs in order to reveal the mechanistic difference between martensitic variant reorientation and detwinning. We used an advanced characterization technique - precession electron diffraction (PED), for the first time for SMAs, to identify the orientation relationships, especially twin planes or junction planes between the adjacent martensite variants.

Bulk $Ni_{50.3}Ti_{29.7}Hf_{20}$ SMA samples were produced via arc melting of high-purity (99.98% Ni, 99.95% Ti, 99.9% Hf) powders, then solution treated at 900 °C for 1 h. Transmission electron microscopy (TEM) specimens were mechanically polished to ~100 μm, using 400-grid to 1200-grid SiC paper, then punched into 3 mm discs. The discs were twin-jet electropolished using a Tenupol-5 polishing system with a solution of 30% nitric acid in ethanol at −30 °C. TEM images were acquired near the perforations using an FEI TECNAI G2 F20 ST FE-TEM at 200 keV. Orientation information was generated using precession electron diffraction (PED, the NanoMEGAS ASTAR system) by recording and analyzing the diffraction pattern at each pixel with a 20 nm step size and a 0.3^{o} precession angle. The diffraction indexing was based on the B19' martensite lattice parameters reported by Evirgen et al. [34]. When presenting the diffraction results in this work, the patterns were not rotated to offset the magnetic rotation of the instrument.

The TEM bright-field image in Fig. 1a shows the representative microstructure of the solution-treated $Ni_{50.3}Ti_{29.7}Hf_{20}$ sample. The sample is fully martensitic at room temperature and many martensite plates are parallel to each other. The corresponding selected-area diffraction pattern (SADP) is provided in Fig. 1b, showing several sets of diffraction spots overlapping. Note that the conventional SADP can help elucidate the overall crystallographic information of the martensite plates. However, the selected area usually contains multiple martensite variants, making revealing the local orientation relationship of the neighboring martensite grains challenging. It is also interesting to note that all martensite plates contain high-density planar defects, as manifested by the unidirectional stripe-like features in each martensite plate. The nature of these planar defects will be discussed shortly. To check whether the samples were fully annealed and solution heat-treated, high-angle annular dark-field scanning transmission electron microscopy (HAADF-STEM) images and diffraction patterns were taken. Neither Z-contrast nano-scale particles nor additional diffraction spots were observed, which ensures the lack of precipitates in these samples.

To reveal the crystallographic information of the internal planar defects and between the martensite plates, PED was employed. In PED, the diffraction pattern of each pixel is recorded. This allows for the correlation of microstructure and diffraction as well as the analysis of orientation relationships [35–38]. Fig. 2a shows the virtual bright-field (VBF) image of an area that contains six parallel martensite plates. (VBF images are constructed based on the intensity of the direct beam in the PED data.) Analysis of the diffraction patterns in the map shows there are four martensite variants. The variants are manually colored in red, blue, yellow, and green, corresponding to variants *A, B, C*, and *D*, respectively. In the selected area, these martensite plates have the *ABCBCD* stacking sequence when examined from top to bottom, separated by solid black lines. From this, one can infer that the martensite variants display strict crystallographic orientation relationships with the twin boundaries or junction planes separating *AB, BC*, and *CD* martensite plates. Note that the colored orientation map (Fig. 2b) does not perfectly correspond to the VBF (Fig. 2a). Even within the same martensite plates, there appear to have interfaces either parallel or at an angle to the twin boundaries or junction planes, leading to different contrasts. A closer inspection of the PED data revealed they are low-angle grain boundaries, which were labeled as the dashed lines in Fig. 2b. These low-angle grain boundaries may result from the relaxation of elastic energy stored adjacent to the boundaries between martensite plates. They also may act as a barrier to twin boundary and junction plane migration during the detwinning process.

We notice that the diffraction patterns from martensite variants *A* and *B* contain the diffraction information from more than one crystal, as shown in Fig. 2c (greyscale diffraction patterns). This indicates that the Ewald sphere intersects with the rel-rods from both the matrix and the twin, which are indicated by the blue and red parallelograms in the diffraction patterns. The twins were indexed as the (0 0 1) compound twin in both variants. The (0 0 1) compound twins were also commonly reported in other NiTi and NiTiHf SMAs [10,14,16,17,19] (also see Table 1).

We further investigate the orientation relationship between the variants, as illustrated in Fig. 2d (colored diffraction patterns). In this diffraction condition, both variants *A* and *B* were tilted to the [1 -1 0] zone axis. The corresponding diffractions exhibit mirror symmetry but do not share a common reflection. This observation indicates that they have a twin relationship but do not have a well-defined low-index twin plane. Combining the diffraction patterns in Fig. 2d and the atomic model Fig. 3a, the twin plane between variants A and B was identified to

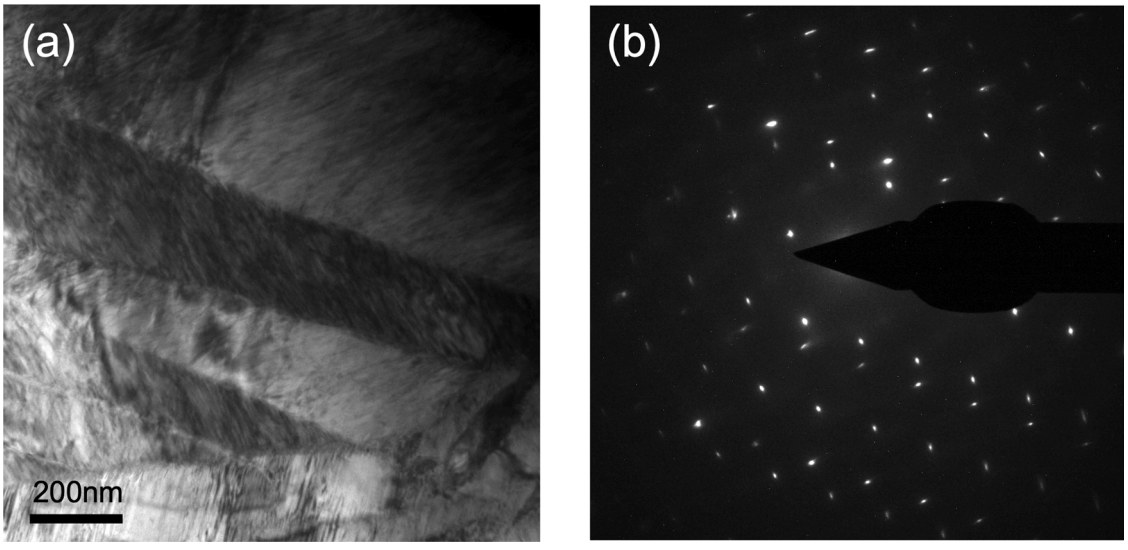

Fig. 1. (a) A bright-field TEM image showing the martensite plate morphology in the solution-treated Ni50.3Ti29.7Hf20 high-temperature shape memory alloy. Note that all martensite plates are highly twinned, (b) the corresponding selected-area diffraction pattern (SADP) from the area shown in (a).

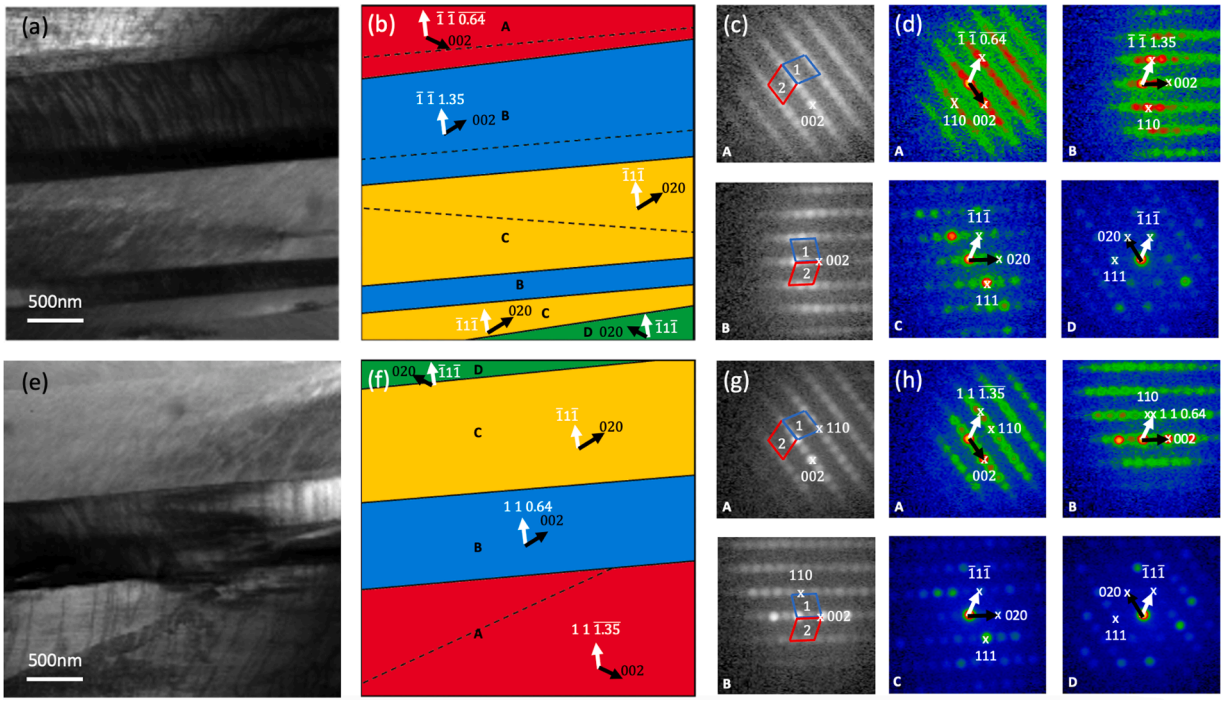

Fig. 2. (a) Virtual bright-field image containing a number of martensite variants in the solution heat-treated Ni50.3Ti29.7Hf20 high temperature shape memory alloy. (b) Corresponding colored map with each orientation assigned with a unique color. The dashed lines are low-angle grain boundaries within the martensite plates. (c) Diffraction patterns for variants A and B show the internal compound twins, highlighted by the blue and red parallelograms. (d) Colored diffraction patterns of four martensite variants A, B, C, and D to elucidate the orientation relationship. Black arrows indicate g-vectors, whereas the white arrows only show the directions with no diffract spot excited. (e)-(h) correspond to (a)-(d) but in a different area of the specimen to highlight the consistency and repeatability of the orientation relationship between the martensite plates.

Table 1
Twin modes reported in NiTi and NiTi-based shape memory alloys from this work and the literature. The ◯* sign indicates the predominant twin mode.

Material	Ref	(0 0 1) Compound	(1 0 0) Compound	{0 1 1} Type I	{1 1 -1} Type I	(1 -1 1) Type I	<0 1 1> Type II	(1 -1 0.64) Type II
$Ni_{50.3}Ti_{29.7}Hf_{20}$	Present work	◯				◯		◯
$Ni_{51}Ti_{49}$ (SHT)	[10]				◯		◯	
$Ni_{51}Ti_{49}$ (Aged)	[10]	◯*						
$Ni_{50}Ti_{50}$	[11]	◯	◯	◯	◯		◯*	
$Ni_{50}Ti_{50}$	[12]	◯		◯	◯		◯	
$Ni_{48.5}Ti_{36.5}Hf_{15}$	[13]	◯*		◯				◯
$Ni_{49}Ti_{36}Hf_{15}$	[14]			◯		◯	◯*	
$Ni_{49.5}Ti_{41.5}Hf_{10}$	[16]	◯*		◯			◯	
$Ni_{50.3}Ti_{29.7}Hf_{20}$	[17, 20]			◯*				
$Ni_{50.3}Ti_{34.7}Hf_{15}$	[18]	◯*		◯*		◯		
$Ni_{50.3}Ti_{29.7}Hf_{20}$	[19]	◯		◯				
$Ni_{44}Ti_{36}Hf_{15}Cu_5$	[39]	◯*		◯*		◯	◯	

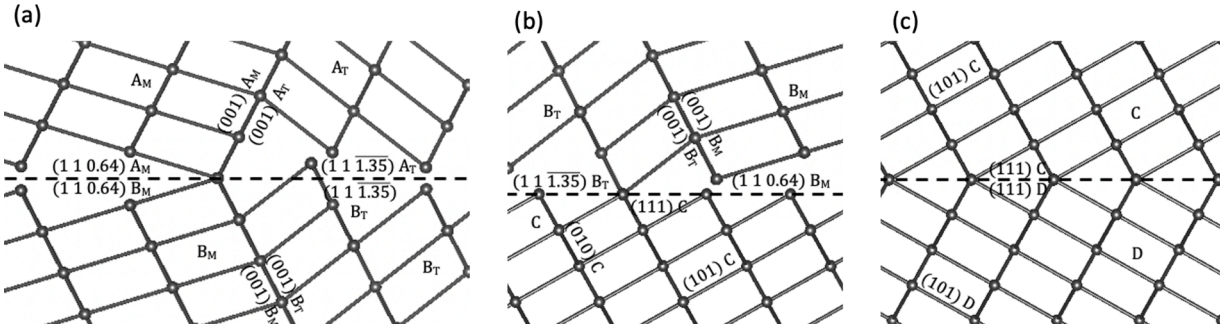

Fig. 3. Atomic models for twins inside and between martensite variants of (a) A and B, (b) B and C, and (c) C and D, presented in Fig. 2.

be either (1 1 0.64) or (1 1 -1.35). These two directions were marked as white arrows in Fig. 2d. (The *g*-vectors pointing to specific reflections were marked by black arrows.) Considering the internal (0 0 1) compound twins in each variant, there are matrices and twins in both *A* and *B* variants. The twin planes separating *A* and *B* are indexed as (1 1 -1.35) for both twinned regions and (1 1 0.64) for both matrix regions (also see Fig. 3a). Note the matrix in *A* does not have a twin relationship with the twin in *B*, and vice versa. This type of twin was not commonly observed in NiTi and NiTiHf SMAs [10-12,15,17-19] and was only reported in a Ni-lean $Ni_{48.5}Ti_{37.5}Hf_{15}$ SMA [16] (refer to Table 1).

It is challenging to unambiguously identify the orientation relationship and the crystal symmetry information between the variants *B* and *C*. Hence, we call the interface "junction plane" [16]. In this diffraction condition, variant B is oriented along the [1 -1 0] zone axis, but variant *C* [1 0 -1] (Fig. 2d). Note that all martensite plates contain high-density (0 0 1) compound twins but only one set of diffraction patterns was revealed in variant *C*. This suggests that only the matrix rel-rods intersect with the Ewald sphere, whereas the twin rel-rods do not. Moreover, no apparent projection of the junction plane was observed, indicating the interface is aligned close to the electron beam direction. A closer inspection of the diffraction patterns of variants *B* and *C* do not exhibit mirror symmetry. Combining the diffraction information and the atomic model in Fig. 3b, it is evident that the (-1 1 -1) plane in variant *C* is parallel to the (1 1 -1.35) twin and (1 1 0.64) matrix in *B*. If the junction plane is parallel to the incident electron beam, the junction plane then can be described based on the crystallographic information above.

Similar to variant *C*, variant *D* has only the matrix reflections excited, and the twin reflections are not visible. The variant *D* is also tilted to the [1 0 -1] zone axis. Variants *C* and *D* exhibit clear mirror symmetry and share the (1 1 1) reflection. Hence the twin type can be identified as the (1 -1 1) Type I twin. This orientation relationship is further illustrated by the atomic model shown in Fig. 3c. Since the common zone axis of variants C and D is [1 0 -1], the (0 0 1) plane does not undergo Bragg diffraction, the internal (0 0 1) twins are not shown in the diffraction patterns in Fig. 2d and the atomic model in Fig. 3c. The (1 -1 1) Type I twin has been observed in some NiTiHf, and NiTiHfCu alloys [15,39] (also refer to Table 1).

To ensure our observation is repeatable, we also acquired additional maps in other areas of the sample and presented one more set of PED results in Fig. 2e-h. In this example, the martensite stacking sequence is *DCBA*. The orientation relationships between *AB, BC*, and *CD* are consistent with the descriptions above.

To compare the martensite variant orientation relationship we uncovered in this work to other binary and ternary NiTi-based SMAs, we summarized the twin types in Table 1. In literature, we note that the predominant twin type is {0 1 1} Type I. The (1 -1 1) Type I and <011> Type II twins were sometimes observed. The {11-1} Type I twins only appear in the NiTi binary SMAs and were not reported in ternary and quaternary SMAs. The (1-1 0.64) Type II twin is the least common. In our solution-treated $Ni_{50.3}Ti_{29.7}Hf_{20}$ sample, only the (1 -1 1) Type I and (1 -1 0.64) Type II twins (also the junction plane between variants *B* and *C*) were observed. None is the predominant type in other SMAs. This is probably due to the very slight B19' lattice distortion from the Hf addition [14] and the absence of precipitates (hence the absence of the associated elastic stress field around the precipitates).

The uncommon twin and junction plane types as well as the low-angle grain boundaries observed in $Ni_{50.3}Ti_{29.7}Hf_{20}$, may explain the transformation strain differences between NiTiHf and NiTi [20–28]. We revealed that, in the solution-treated $Ni_{50.3}Ti_{29.7}Hf_{20}$, (1 1 0.64) Type II twins, a special junction plane, and (1 1 1) Type I twins are present. In contrast, <011> Type II twins are prevalent in NiTi alloys. Different twin and interface types are expected to have different mobilities. Hence, NiTiHf and NiTi should have different detwinning capabilities, which contributes to different transformation strains. Moreover, the presence of the low-angle grain boundaries may retard the twin boundary and junction plane migration, which could also lead to the relatively lower transformation strains observed in NiTiHf.

In summary, we performed microstructure and sub-structure characterization of the solutionized $Ni_{50.3}Ti_{29.7}Hf_{20}$ SMA and revealed the orientation relationship within and between the martensite variants. The key observations can be summarized as follows: (1) the predominant microstructure is the parallel martensite plates with thickness varying from 200 nm to 2 μm. (2) Low-angle grain boundaries within the martensite plates were revealed by PED, which may be mistakenly identified as martensite variant boundaries by regular TEM imaging. (3) All martensite plates contain high-density (0 0 1) compound twins. (4) Four martensite variants observed among the parallel martensite plates are identified as the (1 1 0.64) Type II twin boundaries, a type of junction planes, and the (1 1 1) Type I twin boundaries. (5) These uncommon twin planes, junction planes, and low-angle grain boundaries are the possible reasons for lower transformation strains in NiTiHf than NiTi.

Declaration of Competing Interest

The authors declare that they have no known competing financial interests or personal relationships that could have appeared to influence the work reported in this paper.

Acknowledgments

The authors would like to acknowledge the funding support from the National Science Foundation (NSF-DMR, grant number: 2004752, program manager: Judith Yang) for the financial support for this research. The authors also would like to acknowledge the instrument and technical support from the Microscopy and Imaging Center at Texas A&M University.

References

[1] H. Karaca, et al., Mater. Sci. Technol. 30 (13) (2014) 1530–1544.
[2] G. Firstov, J. Van Humbeeck, Y.N. Koval, Mater. Sci. Eng. 378 (1-2) (2004) 2–10.
[3] M. Zarinejad, Y. Liu, T.J. White, Intermetallics 16 (7) (2008) 876–883.
[4] M. Prasher, et al., Mater. Chem. Phys. 247 (2020), 122890.
[5] J. Ma, I. Karaman, R.D. Noebe, Int. Mater. Rev. 55 (5) (2010) 257–315.
[6] I.D.N. AbuJudom, et al., Google Patents, 1992.
[7] D. Angst, P. Thoma, M. Kao, J. Phys. IV 5 (C8) (1995). C8-747-C8-752.
[8] S. Besseghini, E. Villa, A. Tuissi, Mater. Sci. Eng. 273 (1999) 390–394.
[9] P.E. Thoma, J.J. Boehm, Mater. Sci. Eng. 273 (1999) 385–389.
[10] O. Benafan, et al., Intermetallics 50 (2014) 94–107.
[11] M. Nishida, C. Wayman, A. Chiba, Metallography, 21 (3) (1988) 275–291.
[12] M. Nishida, et al., Acta Metall. Mater. 43 (3) (1995) 1219–1227.
[13] K. Madangopal, R. Banerjee, Scr. Metall. Mater. 27 (11) (1992) 1627–1632.
[14] X. Han, et al., Acta Mater. 44 (9) (1996) 3711–3721.
[15] Y. Zheng, L. Zhao, H. Ye, Scr. Mater. 38 (8) (1998) 1249–1253.
[16] H. XD, et al., Mater. Trans. 38 (10) (1997) 842–851. JIM.
[17] Q. Wei, X. Han, Z. Zhang, Mater. Lett. 60 (25-26) (2006) 3054–3058.
[18] H. Karaca, et al., Acta Mater. 61 (19) (2013) 7422–7431.
[19] R. Santamarta, et al., Acta Mater. 61 (16) (2013) 6191–6206.
[20] A.P. Stebner, et al., Acta Mater. 76 (2014) 40–53.
[21] S. Miyazaki, K. Otsuka, Y. Suzuki, Scr. Metall. 15 (3) (1981) 287–292.
[22] S. Miyazaki, et al., Scr. Metall. 17 (9) (1983) 1057–1062.
[23] K. Gall, et al., Acta Mater. 47 (4) (1999) 1203–1217.
[24] H. Sehitoglu, et al., Metall. Mater. Trans. A 34 (1) (2003) 5–13.
[25] X. Meng, et al., Mater. Lett. 55 (1-2) (2002) 111–115.
[26] G. Bigelow, et al., Scr. Mater. 64 (8) (2011) 725–728.
[27] A. Evirgen, et al., Acta Mater. 83 (2015) 48–60.
[28] L. Patriarca, H. Sehitoglu, Scr. Mater. 101 (2015) 12–15.
[29] H. Sehitoglu, et al., Shape Memory Superelast. 3 (2) (2017) 168–187.
[30] D. Coughlin, et al., Scr. Mater. 67 (1) (2012) 112–115.
[31] F. Yang, et al., Acta Mater. 61 (9) (2013) 3335–3346.
[32] L. Casalena, et al., Microsc. Microanal. 21 (S3) (2015) 607–608.
[33] T. Yu, et al., Acta Mater. 208 (2021), 116651.
[34] A. Evirgen, et al., Acta Mater. 121 (2016) 374–383.
[35] P.A. Midgley, A.S. Eggeman, IUCrJ 2 (1) (2015) 126–136.
[36] D. Yadav, et al., Scr. Mater. 194 (2021), 113677.
[37] K.Y. Xie, et al., Materialia 15 (2021), 101044.
[38] X. Ma, et al., Mater. Res. Lett. 8 (9) (2020) 328–334.
[39] X. Meng, et al., Acta Mater. 58 (10) (2010) 3751–3763.